



OPEN

## Formamidinium lead iodide perovskite photovoltaics with MoS<sub>2</sub> quantum dots

Ankur Uttam Kambley<sup>1✉</sup>, Bruno Alessi<sup>2</sup>, Calum McDonald<sup>2</sup>, Pagona Papakonstantinou<sup>1</sup>, Vladimir Svrcek<sup>2</sup> & Davide Mariotti<sup>3✉</sup>

We present the formation of a composite film made out of formamidinium lead iodide (FAPbI<sub>3</sub>) and molybdenum disulphide quantum dots (MoS<sub>2</sub> QDs) and propose a corresponding photovoltaic device architecture based on a 'type-I' alignment of the two materials' electronic energy levels. The introduction of the MoS<sub>2</sub> QDs has not compromised the overall crystallinity of the FAPbI<sub>3</sub> film and the composite absorber has shown improved stability. We report on the benefits of this composite film and energy band arrangement as the photogenerated carriers in MoS<sub>2</sub> QDs, both positive and negative, are injected into the FAPbI<sub>3</sub> host matrix, resulting in an increased current density of 24.19 mA cm<sup>-2</sup> compared to a current density of 19.83 mA cm<sup>-2</sup> for the control device with FAPbI<sub>3</sub> only. The corresponding photoconversion efficiency increases from 12.6 to 15.0%. We also show that inclusion of MoS<sub>2</sub> QDs in FAPbI<sub>3</sub> films resulted in a notable improvement in the fill factor and open-circuit voltage of the solar cells. Most importantly, MoS<sub>2</sub> QDs enhanced the film stability by reducing defect formation and acting as passivating agents that minimize recombination losses and improve charge carrier transport. Our results suggest that a composite film in a type-I device architecture can introduce benefits for both future developments in perovskite solar cells and effectively tackling the longstanding challenges of carrier transport in QDs solar cells.

The development of next generation solar cells has witnessed tremendous progress in the past 15 years with the introduction of organometal halide perovskites (OHP) as contenders to silicon-based absorbers. Initial efforts in perovskite solar cells (PSCs) yielded certified efficiencies below 15% in 2013, well below silicon-based technologies<sup>1</sup>. Fortunately, despite the much lower efficiencies, scientific progress was supported by the research community, with PSCs now offering a viable alternative to current commercial photovoltaic technologies.

Today, PSCs are close to match the performance of well-established silicon based cells or reach even higher efficiencies in tandem with silicon<sup>1-4</sup>. In addition, the low cost of solution-processing of OHPs makes it an attractive choice for manufacturing. Among PSCs, devices with formamidinium lead iodide (FAPbI<sub>3</sub>, CH<sub>3</sub>(NH<sub>2</sub>)<sub>2</sub>PbI<sub>3</sub>) have shown a very competitive performance<sup>5</sup>. Pb-based OHPs are attractive for photoconversion applications due to their high absorption coefficients<sup>6</sup>, non-radiative recombinations<sup>7</sup>, long carrier diffusion lengths<sup>8</sup>, bandgap tunability and low exciton binding energy<sup>9</sup>. Despite the advantages, Pb-based PSCs have poor shelf life compared to already established silicon-based solar cells because of their sensitivity to moisture and oxygen, which induces degradation of the perovskite film into lead iodide (PbI<sub>2</sub>)<sup>10,11</sup>. The replacement of Pb is always at the expenses of device performance and, the possibility of boosting photocurrent, while using lead-free perovskites, is an attractive and active research topic.

Substantial progress has been made also in other photovoltaic technologies, and for instance researchers have made impressive steps forward in both organic solar cells as well as in quantum dots (QDs) solar cells<sup>1,12,13</sup>. Since 2013, organic solar cells have improved their efficiencies from below 12% to above 19% while QD solar cells have reached also efficiencies above 19% with an impressive jump from below 8%<sup>1</sup>. Furthermore, QD solar cells, which have shown improvements in par with PSCs, do offer the additional potential of overcoming the Shockley-Queasier limit through carrier multiplication<sup>14,15</sup>. However, despite very impressive efforts<sup>16</sup>, one of the main obstacles of QD solar cells remains the 'complicated' carrier transport. In current QD device architectures, carrier transport is necessarily limited by boundary interfaces of the QDs as devices rely on the formation of QDs percolating networks and type-II band alignment (e.g. single-junction, bulk heterojunction)<sup>14</sup>.

<sup>1</sup>School of Engineering, Ulster University, York Street, Belfast BT15 1ED, UK. <sup>2</sup>Renewable Energy Research Center, National Institute of Advanced Industrial Science and Technology (AIST), Tsukuba, Ibaraki 305-8568, Japan. <sup>3</sup>Department of Design, Manufacturing & Engineering Management, University of Strathclyde, Glasgow, UK. ✉email: kambley.a1@gmail.com; davide.mariotti@strath.ac.uk

In order to overcome the limitations of current QD devices, we have recently introduced the possibility of exploiting 'type-I' alignment of energy levels<sup>11</sup>, therefore suggesting a different approach to QD solar cell architectures that can facilitate the exploitation of carrier multiplication. At the same time, the new device architecture with QDs, represent a new avenue that could also introduce important opportunities in perovskite technologies.

In the proposed 'type-I device architecture', the wider bandgap QDs are localised and distributed inside a narrower bandgap bulk semiconductor host material, which together form a composite absorber layer of the solar cells without the requirement for QDs to form percolating networks. The QDs and the semiconductor host material are expected to form an 'atypical' band alignment resulting in a type-I heterojunction. We previously demonstrated the use of silicon nanocrystals as the wider bandgap QDs and methylammonium lead iodide (MAPI) OHP films as narrower bandgap material, which resulted in a current density ( $J_{sc}$ ) of 16 mA cm<sup>-2</sup> compared to a  $J_{sc}$  of 10 mA cm<sup>-2</sup> for a MAPI-only absorber film<sup>11</sup>. Another interesting property of type-I architecture is the possibility of electronic and optical coupling internally in the absorber layer which could lead to carrier multiplication<sup>17–20</sup>. The electronic-coupling occurs when both carriers are generated from both the QDs and the host material via direct photoexcitation and the carriers are extracted from the QDs to the narrower bandgap host material due to type-I alignment. Alternatively optical-coupling occurs when the photoexcited carriers in the QDs go through radiative recombination which releases energy in the form of photons and subsequently these photons cause photoexcitation of carriers in the surrounding narrow-bandgap material. In both coupling cases, the carriers extracted from the absorber layer are a combination of carriers generated from both the QDs and the narrow bandgap material. Therefore, type-I architecture provides a novel approach for solar cell performance enhancement drastically reducing the restriction and limitation of current QD solar cells.

Molybdenum disulphide (MoS<sub>2</sub>) is an attractive material in this context as it exhibits an exceptionally high absorption coefficient and fast carrier dynamics leading to lower recombination rates<sup>21,22</sup>. Bulk MoS<sub>2</sub> is reported to have a bandgap of 1.2 eV while quantum confined MoS<sub>2</sub> nanostructures, with a larger bandgap, have also been explored for a range of applications<sup>23–28</sup>. The vertical alignment of MoS<sub>2</sub> layers in MoS<sub>2</sub> QDs is also reported to assist in perovskite crystallization resulting in enhanced crystallinity and passivation of interfacial defects leading to enhanced performance of the solar cell<sup>29</sup>. Inclusion of MoS<sub>2</sub> nanosheets in perovskite film has also shown to promote oriented crystal growth and high crystal-phase purity reducing the lattice stress of the perovskite film<sup>30</sup>, resulting in higher photovoltaic performance and overall shelf lifetime. A commonly used hole transport layer in PSCs is lithium (Li) doped Spiro-OMeTAD films. MoS<sub>2</sub> nanocrystals have also been reported to be an absorbent of Li<sup>+</sup> ions, thereby suppressing migration of Li<sup>+</sup> ions from the hole transport layer to the perovskite layer resulting in reduced current hysteresis and increased open-circuit voltage ( $V_{oc}$ )<sup>31,32</sup>. Therefore, MoS<sub>2</sub> nanostructures have been proved to be beneficial in a wide range of aspects for PSCs, including film crystallisation, interface passivation and hysteresis suppression. These aspects make MoS<sub>2</sub> nanostructure a prime candidate that could prove highly beneficial in a type-I device architecture within a FAPI layer.

In this paper, we demonstrate the feasibility and successful fabrication of stable FAPI/MoS<sub>2</sub> QDs composite films and provide a comprehensive materials characterization. The MoS<sub>2</sub> QDs were added to the FAPI precursor solution in the concentrations of 0.5 mg mL<sup>-1</sup>, 1 mg mL<sup>-1</sup> and 1.5 mg mL<sup>-1</sup> and detailed FAPI and FAPI/MoS<sub>2</sub> QDs film properties are presented. The charge carrier transport has been studied by evaluating the energy band diagrams (EBDs). We demonstrate that FAPI and MoS<sub>2</sub> QDs form a type-I alignment that allows us to demonstrate the proposed type-I device architecture. We therefore report enhanced performance of FAPI/MoS<sub>2</sub> QDs solar cells. The highest power conversion efficiency (PCE) of 15.01% was achieved with 1 mg mL<sup>-1</sup> MoS<sub>2</sub> QDs in FAPI film compared to PCE of 12.59% in the case of FAPI-only device.

## Results and discussion

### Material characterisation and energy band diagram evaluation

Here we refer to the different films as FAPI (FAPI only without MoS<sub>2</sub> QDs), FAPI 0.5 (with 0.5 mg mL<sup>-1</sup> MoS<sub>2</sub> QDs), FAPI 1 (with 1 mg mL<sup>-1</sup> MoS<sub>2</sub> QDs) and FAPI 1.5 (with 1.5 mg mL<sup>-1</sup> MoS<sub>2</sub> QDs). The morphology of the films with the MoS<sub>2</sub> QDs, see Fig. S2b–d in the supporting information (SI), appear more compact and homogeneous compared to the FAPI only films (Fig. S2a in SI) with clearer and large grains. In the literature, it has been reported that MoS<sub>2</sub> QDs assists in enhanced crystallinity of perovskite films and passivated interfacial defects<sup>29</sup>. The thickness of the films was examined by SEM from the films cross-sections (Fig. S3 in SI), which reported very similar values for all the films at the different MoS<sub>2</sub> QDs concentrations. Average thickness values were 771 nm, 740 nm, 766 nm and 659 nm for the FAPI, FAPI 0.5, FAPI 1 and FAPI 1.5 respectively.

Further detailed X-ray photoelectron spectroscopy (XPS) analysis was conducted on the FAPI 1.5 film to examine the chemical composition of the FAPI/MoS<sub>2</sub> film. FAPI 1.5 was chosen as it contains highest amount of MoS<sub>2</sub>. The peaks corresponding to Pb 4f and I 3d as well as those corresponding to O 1s, C 1s and N 1s were analysed (Fig. 1) as related to the chemical formula for FAPI, CH<sub>3</sub>(NH<sub>2</sub>)<sub>2</sub>PbI<sub>3</sub><sup>33</sup>. Deconvolution of the peaks corresponding to Pb 4f<sub>7/2</sub> and Pb 4f<sub>5/2</sub> orbitals (Fig. 1a) indicated the presence of Pb<sup>2+</sup> and Pb<sup>3+</sup> oxidation states. The Pb 4f<sub>7/2</sub> and Pb 4f<sub>5/2</sub> spin-orbital peaks corresponding to Pb<sup>3+</sup> are located at 137.7 eV and 142.6 eV, respectively (Fig. 1a). In the literature, these peaks are associated to  $\delta$ -FAPI phase<sup>34</sup>. The I 3d orbital spectrum (Fig. 1b) shows I 3d<sub>5/2</sub> and I 3d<sub>3/2</sub> spin-orbitals at 620.3 eV and 631.9 eV respectively<sup>34</sup>. The Pb<sup>3+</sup> peaks from Pb 4f orbital spectrum and I 3d orbital peaks are characteristic peaks for FAPI<sup>35,36</sup>. The Pb 4f<sub>7/2</sub> and Pb 4f<sub>5/2</sub> spin-orbital peaks, corresponding Pb<sup>2+</sup> oxidation state are located at 139.4 eV and 144.2 eV respectively (Fig. 1a). These peaks indicate the formation of Pb(CO<sub>3</sub>)<sub>2</sub> due to the adsorption of atmospheric CO<sub>2</sub><sup>37,38</sup>. Formation of Pb(CO<sub>3</sub>)<sub>2</sub> is also corroborated from the deconvolution of O 1s (Fig. 1c) and C 1s (Fig. 1d). The deconvolution of O 1s orbital spectrum indicates peaks corresponding to C=O (531.7 eV) and O=C–O (533.1 eV)<sup>39</sup>. Deconvolution of C 1s orbital spectrum shows peaks corresponding to C–C (284.8 eV) adventitious (aliphatic) carbon, C–N/C–OH (286 eV) and C–O (287.1 eV)<sup>39</sup>.

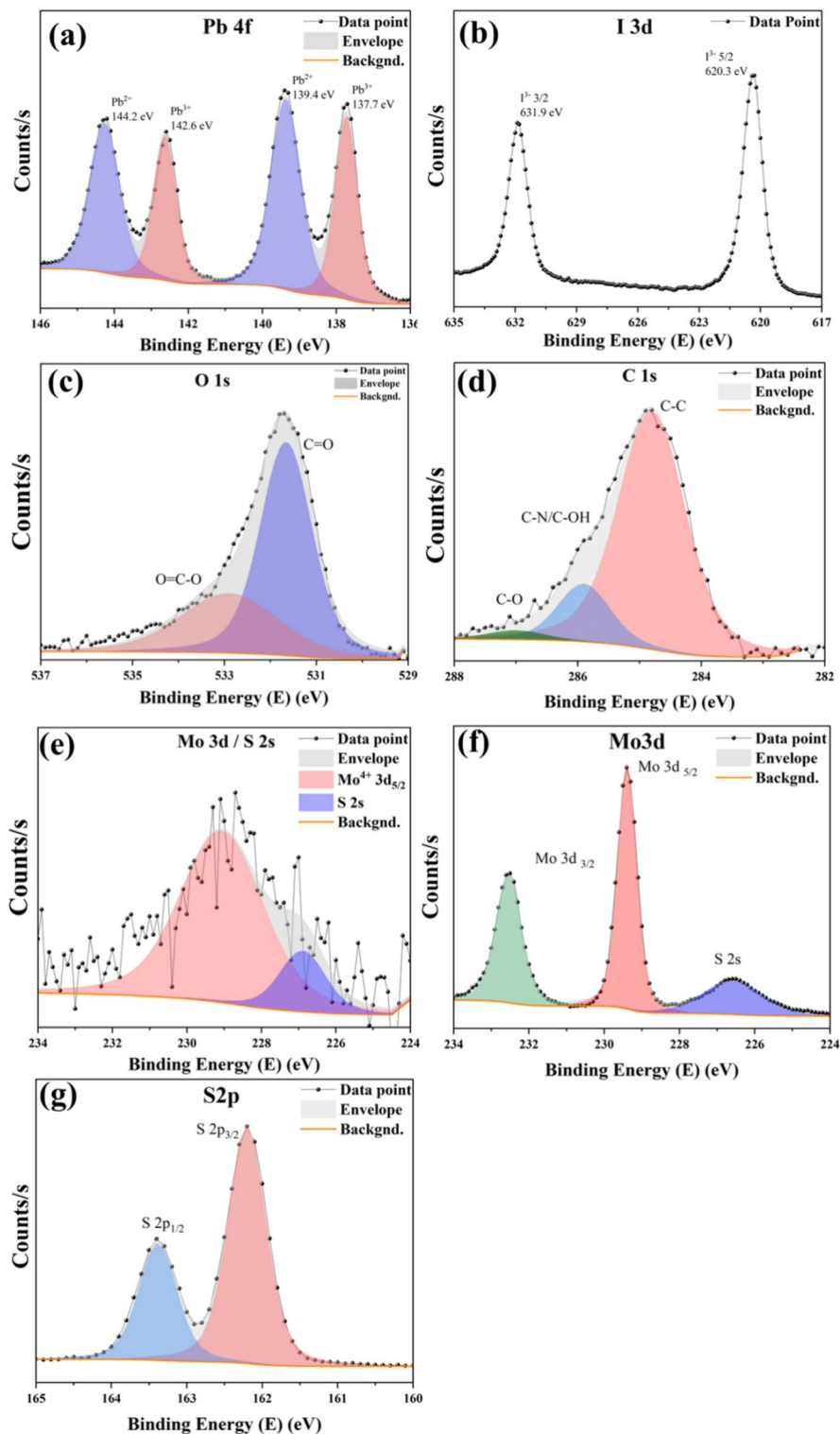


**Fig. 1.** XPS spectra for FAPI 1.5 film showing (a) Pb 4f showing  $\text{Pb}^{2+}$  and  $\text{Pb}^{3+}$  (FAPI) peaks, (b) I 3d orbital showing FAPI related peaks, (c) O 1s orbital, (d) C 1s orbital and (e) Mo 3d/S 2s orbital. The XPS spectra for drop-casted  $\text{MoS}_2$  QDs showing (f) Mo 3d orbital and (g) S 2p orbitals.

The presence of  $\text{MoS}_2$  QDs in the FAPI 1.5 film was confirmed by Mo 3d orbital spectrum (Fig. 1e) obtained from conducting XPS on the films. The deconvolution of Mo 3d spectrum reveals the presence of  $\text{Mo}^{4+}$  oxidation state as referred to Mo  $3d_{5/2}$  spin-orbital peak located at 228.29 eV and S 2s spin orbital peak located at 226.31 eV.

These peaks are characteristic peaks for MoS<sub>2</sub><sup>33</sup>. For comparison, XPS was performed also on drop-casted MoS<sub>2</sub> QDs on a gold-coated silicon wafer from a colloid in dimethylformamide (DMF). The gold layer was grounded with the XPS stage. Deconvolution of the Mo 3d peak shows Mo 3d<sub>5/2</sub> (229.39 eV), Mo 3d<sub>3/2</sub> (232.54 eV) and S 2s (226.60 eV) peaks related to Mo–S bonds (Fig. 1f)<sup>40–42</sup>. Similarly as shown in Fig. 1g, the doublet S 2p<sub>3/2</sub> at 162.20 eV and S 2p<sub>1/2</sub> at 163.39 eV represent Mo–S bonds<sup>43,44</sup>. These results confirm the chemical composition and stability of the MoS<sub>2</sub> QDs without an oxide or a metallic component.

The Raman spectrum of MoS<sub>2</sub> QDs, Fig. 2a, shows the E<sub>2g</sub><sup>1</sup> mode (in-plane vibrations) at 377.40 cm<sup>-1</sup> and A<sub>1g</sub> mode (out-of-plane vibrations) at 402.13 cm<sup>-1</sup>. The Raman spectrum corresponding to FAPI 1.5 film (Fig. 2b) shows the presence of E<sub>2g</sub><sup>1</sup> mode at 398.23 cm<sup>-1</sup> and A<sub>1g</sub> mode at 421.59 cm<sup>-1</sup>. The difference ( $\Delta f$ ) between Raman modes is  $\Delta f = 23.73$  cm<sup>-1</sup> for MoS<sub>2</sub> QDs and  $\Delta f = 23.36$  cm<sup>-1</sup> for FAPI 1.5 film. In the literature,  $\Delta f$  values of 24.4 cm<sup>-1</sup>, 25.7 cm<sup>-1</sup> and 25.9 cm<sup>-1</sup> are reported for MoS<sub>2</sub> QDs<sup>45–47</sup>. The  $\Delta f$  value provides an estimate of the number of layers in MoS<sub>2</sub> QDs, with higher values indicating fewer number of layers as fewer layers result in less-stiffening of the vibrations. In the case of our work, the  $\Delta f$  value for FAPI 1.5 film is lower as compared to only MoS<sub>2</sub> QDs. This indicates stiffening of both out-of-plane and in-plane vibrations in FAPI 1.5 film, which is reasonable as MoS<sub>2</sub> QDs are embedded into the FAPI matrix. Similarly, this effect can also be noticed from the red-shift of the individual E<sub>2g</sub><sup>1</sup> and A<sub>1g</sub> modes in the case of FAPI 1.5 film. The red-shift has been also reported to be associated with stiffening of the Mo–S bond vibrations<sup>46,47</sup>.

The optical properties were examined by analysing absorbance and absorption coefficient of the films. It should be noted that the measurements are impacted due to fast degradation of the films. As shown in Fig. 3a, absorbance is in the range of 400–800 nm which is consistent with the characteristics of good quality FAPI based films<sup>48</sup>. FAPI 0.5 film shows slightly lower absorbance compared to the FAPI-only film. However, FAPI 1 and FAPI 1.5 show an increase in absorbance compared to FAPI-only. Due to the low concentration of MoS<sub>2</sub>, the difference is relatively small compared to FAPI-only and among the films with different MoS<sub>2</sub> concentrations. The absorption coefficient of the films was calculated with respect to film thicknesses. The film thicknesses were evaluated by a profilometer on different spots on each film (Fig. S4 in SI) and the median value was taken as the final thickness. The thickness of the individual films used for optical characterization was found to be 210 nm, 200 nm, 200 nm, 210 nm for FAPI, FAPI 0.5, FAPI 1 and FAPI 1.5 respectively. The highest absorption coefficient was obtained from FAPI 1 film. The absorption coefficient is of the order of 10<sup>5</sup> cm<sup>-1</sup>, as shown in Fig. 3b, suggesting that 1 mg mL<sup>-1</sup> of MoS<sub>2</sub> QDs concentration is optimal for FAPI-based devices.

The proposed type-I alignment in this work crucially hinges on the position of energy levels of the two materials i.e. FAPI and MoS<sub>2</sub> QDs. The wide bandgap material (MoS<sub>2</sub> QDs) should align with the narrower bandgap material such that photogenerated carriers (electrons and holes) are transported from the MoS<sub>2</sub> QDs to the FAPI layer. To obtain the bandgap, Tauc plots were constructed on the basis of ultraviolet–visible transmittance and reflectance measurement results. In the case of the composite films, direct transition bandgap was observed at 1.533 eV, 1.533 eV, 1.533 eV and 1.531 eV for FAPI, FAPI 0.5, FAPI 1 and FAPI 1.5 respectively (Fig. S6a in SI). These are all very close to the value of 1.53 eV, confirming that the inclusion of MoS<sub>2</sub> QDs has not caused disruption to the FAPI film. For MoS<sub>2</sub> QDs, the direct transition bandgap of 1.63 eV was observed (Fig. S6b in SI). These values are suitable to produce a type-I alignment, whereby the bandgap of the FAPI film could be nested within the larger bandgap of the MoS<sub>2</sub> QDs.

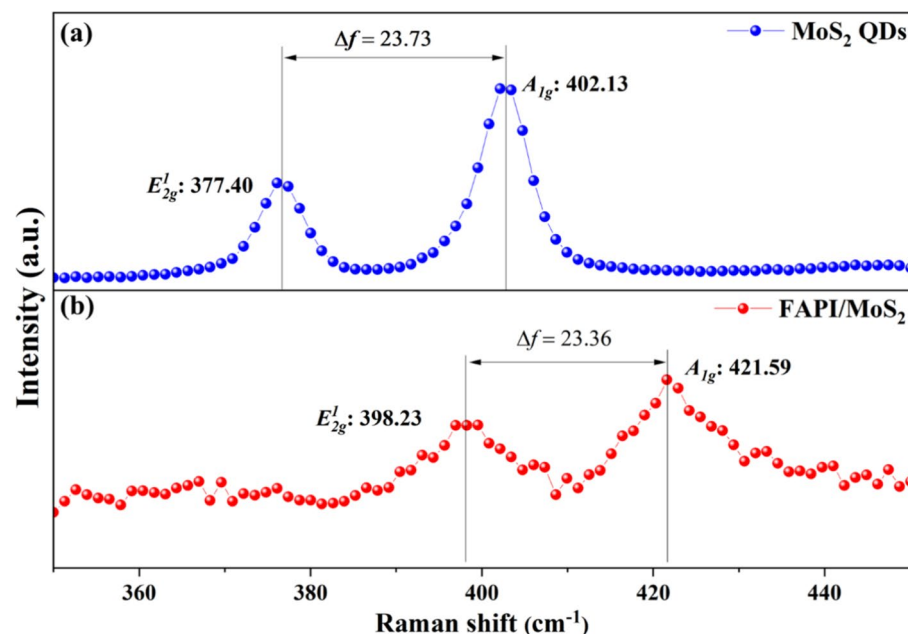


**Fig. 2.** Raman spectrum of the (a) MoS<sub>2</sub> QDs and (b) FAPI 1.5 film with MoS<sub>2</sub> QDs related vibrational peaks.

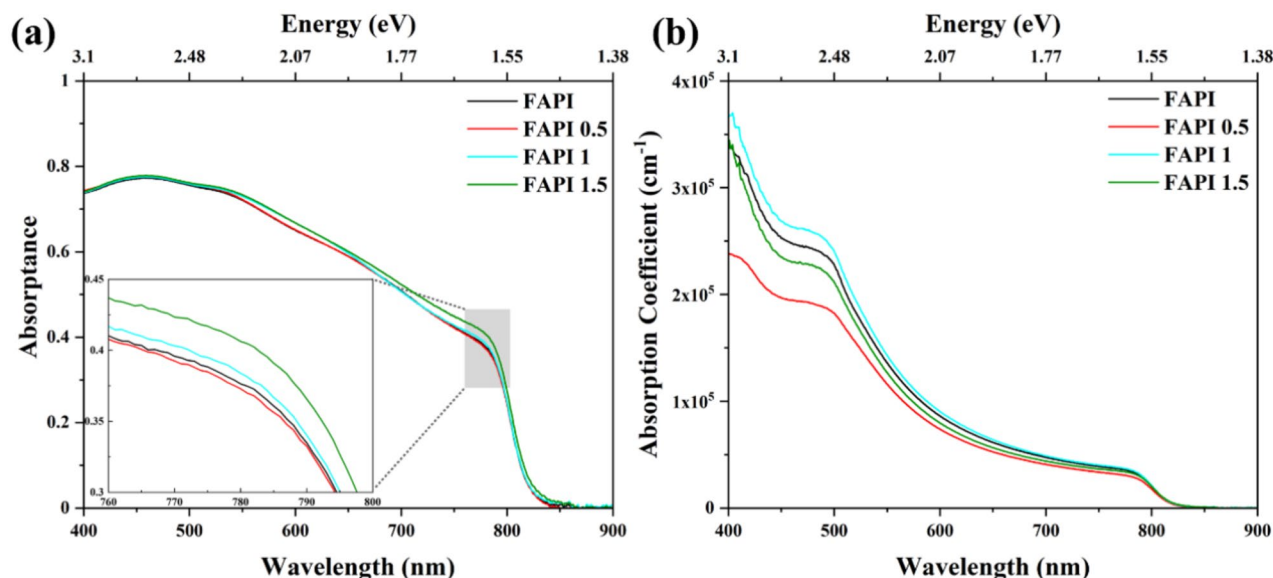


**Fig. 3.** Optical characterisation from UV–Vis measurements of FAPI, FAPI 0.5, FAPI 1 and FAPI 1.5 films showing (a) absorbance and (b) absorption coefficient.

The valence band maximum (VBM) and Fermi level ( $E_f$ ) values for MoS<sub>2</sub> QDs were measured by ultraviolet photoelectron spectroscopy (UPS). The UPS spectrum obtained from MoS<sub>2</sub> QDs is presented in Fig. S5 of the SI. The  $E_f$  level was determined from the cut-off edge of the secondary electrons at 16.45 eV, returning the  $E_f$  value of  $-4.77$  eV. The onset of the spectrum is located at 1.06 V, which returns the difference between VBM and  $E_f$ . Therefore, using the  $E_f$  value obtained, the VBM energy level is estimated at  $-5.83$  eV. The conduction band minimum (CBM) value of the MoS<sub>2</sub> QDs was then calculated from the measurements of the VBM and bandgap, which produced a value of  $-4.2$  eV ( $-5.83$  eV + 1.63 eV). Table 1 shows the summary of the energy band levels for FAPI and MoS<sub>2</sub> QDs (values for FAPI were taken from the literature).

Based on the energy band positions for FAPI and MoS<sub>2</sub> QDs, Fig. 4a,b shows the energy band diagram (EBD) for FAPI and MoS<sub>2</sub> QDs separately and in equilibrium. A small energy barrier is formed due to the mismatch between Fermi levels. However, these barriers are relatively small and with reduced impact on carrier transport when the absorber layer operates in full depletion under an electric field. Hence good adherence of type-I band alignment is observed between the MoS<sub>2</sub> QDs and FAPI.

### Solar cell architecture and performance

The photovoltaic (PV) architecture was evaluated with SnO<sub>2</sub> as the electron transport layer (ETL), Spiro as the hole transport layer (HTL) and FAPI (or FAPI/MoS<sub>2</sub> QDs) as the absorber layer. Figure 4a,b shows the EBD of the proposed PV architecture of the FAPI/MoS<sub>2</sub> film with all the layers involved.

Figure 4c shows the schematic of the device fabricated on fluorine-doped tin oxide (FTO) coated glass. SnO<sub>2</sub> as ETL, FAPI/MoS<sub>2</sub> film as the absorber layer, spiro as the HTL and Au as the metal contact. The thicknesses of the individual layers in the device were evaluated by scanning electron microscopy (SEM) on the cross-section of the device (Fig. S7b). The thicknesses measured from SEM image for FTO, SnO<sub>2</sub>, FAPI/MoS<sub>2</sub> QDs, spiro and Au are 100 nm, 400 nm, 750 nm, 300 nm and 200 nm, respectively. Energy dispersive X-ray spectroscopy (EDS) maps were obtained for each layer to investigate the chemical composition shown in the SI (Fig. S7d–m). Distinct colour maps are observed for each layer. Furthermore, the EDS line scan was conducted across the device layers, shown in the SI (Fig. S7n). The thicknesses for the individual layers were also obtained, which corroborate well with thicknesses obtained from cross-sectional SEM.

PV devices were fabricated with FAPI only, FAPI 0.5, FAPI 1 and FAPI 1.5 films as the absorber layers. Performance of these devices were evaluated by current density–voltage ( $J$ – $V$ ) characterisation. The active surface area of our devices was  $\sim 23$  mm<sup>2</sup> and a shadow mask was used during illumination. The best performance was observed with the FAPI 1 film, i.e. with 1 mg mL<sup>-1</sup> MoS<sub>2</sub> QD in FAPI. Figure 5a shows the comparison between the champion devices of FAPI only and FAPI 1.

Sample	$E_f$ (eV)	VBE (eV)	$E_g$ (eV)	CBE (eV)
FAPI	$-4.4$	$-5.4$	1.4	$-4$
MoS <sub>2</sub> QDs	$-4.77$	$-5.83$	1.63	$-4.2$

**Table 1.** Summary of energy band values of the FAPI film and MoS<sub>2</sub> QDs.



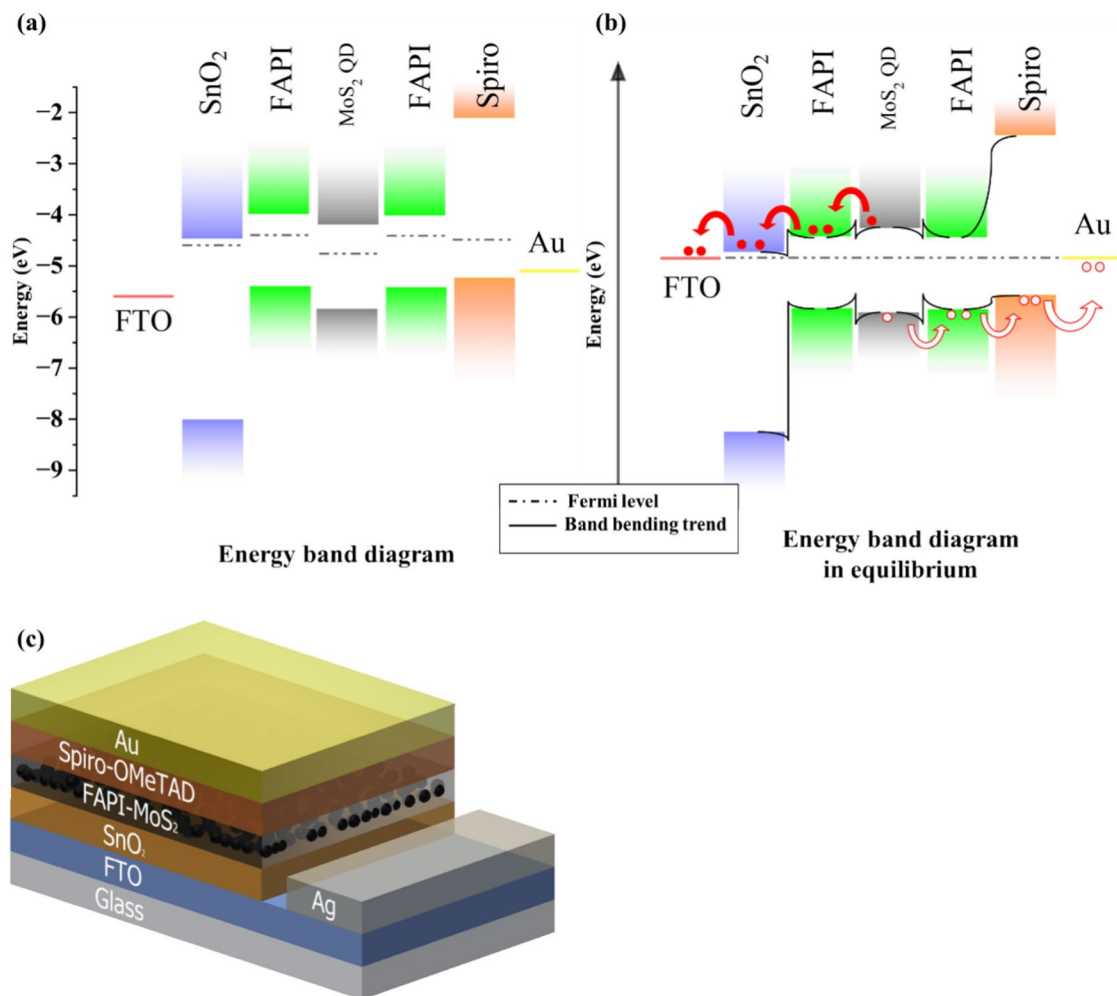


**Fig. 4.** (a) Energy band alignment diagram (EBD) for type-I solar cell with FAPI/MoS<sub>2</sub> as active layer, tin oxide (SnO<sub>2</sub>) as electron transport layer and spiro-OmeTAD as hole transport layer. (b) EBD in equilibrium.

We observed that the FAPI 1 champion device exhibits the highest power conversion efficiency (PCE) of 15.01% as compared to the FAPI-only champion device which exhibits the efficiency of 12.59%. The corresponding devices resulted in  $J_{SC}$ ,  $V_{OC}$  and fill factor (FF) of 24.19 mA cm<sup>-2</sup>, 0.94 V and 0.65 respectively in case of FAPI 1 device. FAPI-only devices resulted in  $J_{SC}$ ,  $V_{OC}$  and FF of 19.83 mA cm<sup>-2</sup>, 0.9 V and 0.52 respectively. The rise in efficiency in the devices, with the inclusion of MoS<sub>2</sub> QDS, could be attributed to enhanced generation and transport of the photogenerated carriers from the MoS<sub>2</sub> QDs and due to type-I architecture, in addition to the photogenerated carriers from FAPI film. Consistently to the J–V curve (Fig. 5a), the external quantum efficiency (EQE, Fig. 5b) of FAPI 1 shows the maximum PCE of around 80% for incident wavelengths in the range of 400–800 nm as compared to 60% for the FAPI only. Unfortunately, as the bandgap value of the two components are very close to each other (1.53 eV for FAPI and 1.63 eV for MoS<sub>2</sub> QDs), it is not possible to clearly see the change in slope of the EQE signal. Corresponding current density calculated from EQE measurements for FAPI only and FAPI 1 devices are 18.94 mA cm<sup>-2</sup> and 23.10 mA cm<sup>-2</sup>, which are sufficiently close to the values obtained from J–V characteristics. Statistics of performance parameters for FAPI only, FAPI 0.5, FAPI 1 and FAPI 1.5 are shown in Fig. 5c–f. The FAPI 0.5 and FAPI 1.5 show relatively low performance overall, confirming the optimal concentration of MoS<sub>2</sub> QDs at 1 mg mL<sup>-1</sup>, whereby different concentrations might either disrupt transport (high concentration) or produce an insufficient contribution to the absorption (low concentration, see also Fig. 3b).

In order to understand the contribution of MoS<sub>2</sub> QDs in the photocurrent we analysed further the EQE measurements. The minority carrier diffusion length ( $L_{diff}$ ) was calculated for the two different devices from the data points of the EQE in the range 800–850 nm. Figure S8a in the SI shows the x-intercept of  $IQE^{-1}$  vs  $\alpha^{-1}$  which gives the  $L_{diff}$  values for FAPI and FAPI 1 of 0.325  $\mu$ m and 0.753  $\mu$ m. The higher minority carrier diffusion length may be attributed to FAPI interface defect passivation and reduction of grain boundaries (e.g. see Fig. S2 in SI) as a result of the MoS<sub>2</sub> QDs inclusion<sup>29</sup>. The inclusion of MoS<sub>2</sub> QDs in FAPI shows more than doubling of the  $L_{diff}$  values, which confirms that the type-I architecture can contribute to improved photogenerated carrier transport. The performance enhancement due to type-I architecture is also corroborated from the J–V dark current analysis, shown in the SI, Fig. S8b. As seen from the space charge region, the device corresponding to

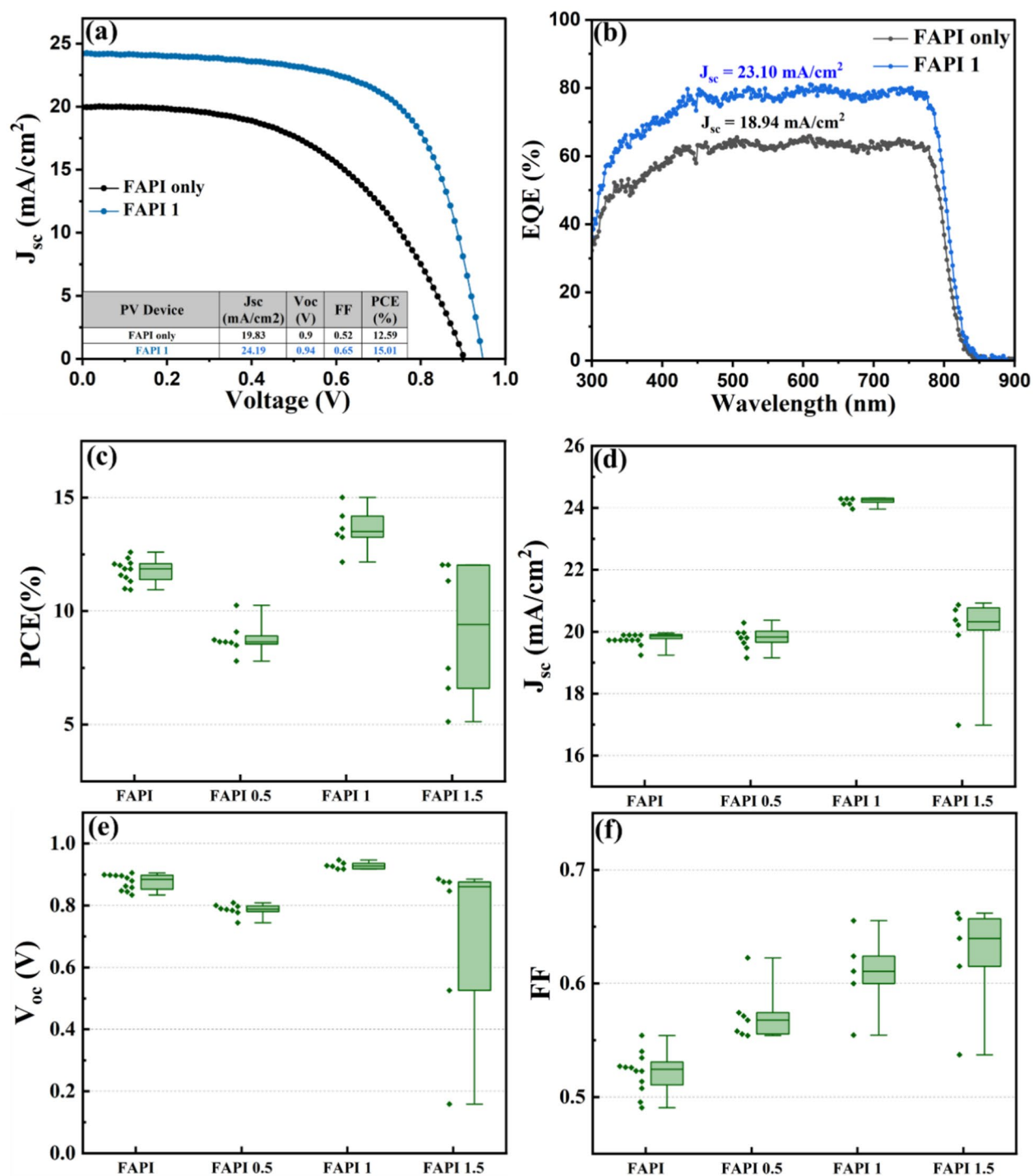


**Fig. 5.** Solar cell performance with type-I device architecture FTO-SnO<sub>2</sub>-perovskite-spiro-Au. (a) Shows the J–V characteristics of champion devices with FAPI and FAPI 1 active layer. (b) EQE of the FAPI and FAPI 1 device. Statistics of performance parameters (c) short-circuit current density ( $J_{sc}$ ), (d) open-circuit voltage ( $V_{oc}$ ), (e) fill factor and (f) photo conversion efficiency (PCE).

FAPI 1 shows higher  $J_{sc}$  in the diffusion region indicating qualitatively higher  $L_{eff}$ . Similarly, the  $J_{sc}$  values in recombination region for FAPI 1 devices is lower compared to FAPI-only indicating lower recombination rates.

## Conclusion

We have successfully produced stable and crystalline composite films of FAPI with MoS<sub>2</sub> QDs. SEM images revealed that the presence of MoS<sub>2</sub> resulted in smaller grains, augmenting the mechanical robustness of the films. The presence of MoS<sub>2</sub> QDs in FAPI was verified through XPS and Raman spectra and the analysis of the energy

band levels reveals a type-I alignment. The use of composite FAPI/MoS<sub>2</sub> QDs films resulted in an enhancement in the efficiency of corresponding devices from 11.76 to 13.61% (average values from statistical analysis). The comparison of carrier diffusion length in FAPI and FAPI/MoS<sub>2</sub> QDs films indicated a higher diffusion length in FAPI/MoS<sub>2</sub> QDs, suggesting that MoS<sub>2</sub> QDs not only contribute to the passivation of interface defects but also improve the transport of photogenerated carriers due to the type-I architecture. Our results demonstrate the feasibility of devices with a type-I architecture, which could benefit from synergies of different materials and provide a realistic avenue for quantum dot solar cells, overcoming the long-standing challenge of carrier transport.

## Experimental details

### Chemicals and materials

Formamidinium iodide (CH<sub>3</sub>IN<sub>2</sub>, purity ≥ 99% anhydrous), methylammonium chloride (CH<sub>3</sub>ClN, purity ≥ 99.0%) and lead (II) iodide (PbI<sub>2</sub>, purity 99.999% trace metals basis) were purchased from Sigma-Aldrich and used as precursors to produce the FAPI films. Dry molybdenum sulphide (MoS<sub>2</sub>) QDs powder was synthesised following a previous reported recipe and procedures<sup>47</sup>. Dimethylformamide (DMF, purity > 99%) and dimethyl sulfoxide (DMSO, purity > 99%) was purchased from Sigma-Aldrich. Tin (IV) oxide (SnO<sub>2</sub>) colloid was purchased from Alfa Aesar, 15% wt in de-ionized (DI) water. Titanium diisopropoxide bis(acetylacetonate), titania paste, butanol (anhydrous, 99.8%), ethanol (anhydrous, ≥ 99.5%), 2,2',7,7'-tetrakis-(N,N-di-4-methoxyphenylamino)-9,9' spirobifluorene (Spiro-OMeTAD), 4-*tert*-butylpyridine (tBP), lithium bis(trifluoromethanesulfonyl)imide (Li-TFSI), isopropyl alcohol and n-octylammonium iodide (OAI) were purchased from Sigma-Aldrich. 15 MΩ cm de-ionized (DI) water is used throughout the process. Fluorine-doped tin oxide (FTO) coated glass substrates were purchased from Visiontek systems. MoS<sub>2</sub> QDs powder is prepared by synthesis process detail in literature<sup>47</sup>.

### Characterisation techniques

Scanning electron microscopy (SEM) was conducted using Hitachi SU5000 microscope. The electron gun was operated at 15 kV under high-vacuum condition. Energy dispersive X-ray spectroscopy (EDS) was performed by an in-situ Oxford Instruments X-max 80 detector. X-ray photoemission spectroscopy (XPS) was performed using an ESCALAB 250 Xi spectrometer (Thermo Fisher Scientific, UK) using a monochromated aluminium anode with an excitation energy of 1486.68 eV. The analysis chamber pressure was maintained at  $1 \times 10^{-9}$  mbar. The samples were prepared by spin coating the FAPI precursor solution on quartz substrate. Charge correction was done against the platinum (Pt) peak at 71.2 eV corresponding to 4f orbital. Pt foil was loaded in the XPS with every sample and was grounded with the stage. The same equipment chamber and detector was used for ultraviolet photoemission spectroscopy (UPS) however with a helium discharge source (He I: 21.2 eV) as excitation to determine the fermi-level ( $E_f$ ) and the valence band maximum (VBM). A negative bias of -10 V was applied to the stage during the measurements. During XPS and UPS analysis the surface of the sample was grounded with the equipment stage. Raman spectroscopy was performed with an inVia™ Qontor™ confocal Raman microscope with 532 nm laser. Ultraviolet–visible spectroscopy (UV–Vis) was performed using a PerkinElmer Lambda 1050+ UV–Vis spectrophotometer with the spectral range of 190–3500 nm. The monochromator was set at 1 nm step size. The equipment was fitted with 150 mm integrating sphere for transmittance and reflectance measurements. The samples for UV–Vis spectroscopy were prepared by spin coating the FAPI precursor solution on quartz substrates. Transmittance ( $T$ ) was obtained by placing the sample in the transmittance port (front-end) of the integrating sphere. Reflectance was measured by placing the sample at reflectance port (back-end on the integrating sphere). The calculation of absorbance, absorption coefficient and bandgap from  $T$  and  $R$  spectra of the films are described in the supporting information (SI, Section S1). The optical properties of MoS<sub>2</sub> QDs were evaluated by performing UV–Vis on colloidal samples of MoS<sub>2</sub> QDs in DMF. Transmittance was obtained by placing the cuvette at the transmittance port. The combined signal of transmittance and scattering ( $T + S$ ) was obtained by placing the cuvette at the centre of the integrating sphere.

The performance of solar cells was tested under AM1.5G solar spectrum with irradiance of 100 mW cm<sup>-2</sup> using Wacom Electric Co. solar simulator (JIS, IEC standard conforming, CLASS AAA). An aperture mask of 0.2275 cm<sup>2</sup> was used to incident the light on the devices. The spectral response was calibrated using an a-Si reference cell. Keithley 2400 source meter was used to record electrical data. The external quantum efficiency (EQE) of the solar cells was measured using an Eko Seiki SPM-005B system in direct current (DC) mode with 150 W Xenon lamp. A a-Si reference cell was used to calibrate the spectral response also in this case. The current density ( $J_{sc}$ ) and the minority carrier diffusion length ( $L_{diff}$ ) were calculated using the EQE data (see SI, Section S2).

### Solar cell fabrication

The step-by-step schematic diagram of the solar cell fabrication process is reported in the SI (Fig. S1). Devices were fabricated on glass substrates coated with fluorine-doped tin oxide (FTO). The substrates were cleaned by sonication in four different solutions for 10 min each in the following order: 2% Hellmanex III solution in DI water, DI water, acetone and ethanol. Substrates then were dried with a nitrogen gun and exposed to 20 min ozone using photo surface processor from SEN LIGHTS Corporation, model pl16-110.

SnO<sub>2</sub> was used as the electron transport layer (ETL). The SnO<sub>2</sub> colloid is diluted by 1:1 volume ratio in water, followed by filtration with 0.22 μm filters. 300 μL of this solution was then spin coated at 3000 rpm for 30 s followed by annealing in air at 150 °C for 30 min. Samples were allowed to cool down to ambient temperature following this and any other annealing process. The substrates with ETL were then treated with ozone for 10 min before depositing the next layer. The deposition of the absorber layer, FAPI without MoS<sub>2</sub> QDs, was carried out in a nitrogen-ventilated glove box where the relative humidity was less than 10%. The precursor solution was prepared by dissolving PbI<sub>2</sub> (1.92 M), CH<sub>3</sub>ClN (0.64 M) and CH<sub>3</sub>IN<sub>2</sub> (1.83 M) in a 4:1 ratio by volume of DMF and DMSO. In order to prepare the composite absorber layer of FAPI with the MoS<sub>2</sub> QDs, different amounts



of the MoS<sub>2</sub> QDs (1.5 mg, 1 mg and 0.5 mg) were dispersed in a solution of DMF and DMSO with a 4:1 ratio by volume. Subsequently, PbI<sub>2</sub> (1.92 M), CH<sub>6</sub>ClN (0.64 M) and CH<sub>5</sub>IN<sub>2</sub> (1.83 M) were added. The colloidal was left on the shaker overnight to thoroughly mix the added powders. The colloid or solution (50 µL) of the absorber layer was spin-coated at 4000 revolution per minute (rpm) for 30 s and 300 µL of antisolvent anisole was dropped from a ~0.7 cm diameter orifice at approximately 20 s in the spin-coating process<sup>49</sup>. The samples were then heated on a hotplate at 150 °C for 15 min. The film visibly crystallises within seconds to form a mirror like black textured finish.

Spiro-OMeTAD was used as the hole transport layer (HTL) and the deposition was continued in the glovebox. The precursor solution was prepared by dissolving 216 mg of Spiro-OMeTAD in chlorobenzene. A 52.5 µL mixture of 39 mg Li-TFSI in 75 µL acetonitrile and 85.5 µL was then added to the Spiro-OMeTAD precursor solution, which was then spin-coated in an N<sub>2</sub>-ventilated glove box where relative humidity was less than 10%. 300 µL of the solution was spin-coated at 4000 rpm for 30 s and was left to dry at room temperature. The devices fabricated and with Spiro-OMeTAD were then stored in a humidity controlled dry box overnight. Au-contacts are deposited on spiro by thermal evaporation of gold wire followed by application of an Ag paste on the underlying FTO layer to form Ag contacts. The total active device surface area was ~23 mm<sup>2</sup> and an aperture mask of 0.2275 cm<sup>2</sup> was used to characterise the devices. The devices were stored in the dry box overnight to allow Ag paste to solidify.

## Data availability

This paper is accompanied by representative samples of experimental data and the relevant numerical tabulated raw data is available from the University of Strathclyde's Research Portal at <https://doi.org/10.15129/864c99bb-a8d0-4528-9ea0-28b0396675a4>. Detailed procedures explaining how these representative samples were selected, and how these experiments can be repeated, are provided in the corresponding sections of this paper. Additional results and raw data underlying this work are available in the Supporting Information or on request following instructions provided at <https://doi.org/10.15129/864c99bb-a8d0-4528-9ea0-28b0396675a4>.

Received: 9 July 2024; Accepted: 3 September 2024

Published online: 16 September 2024

## References

1. NREL Best Research-Cell Efficiency Chart. <https://www.nrel.gov/pv/assets/pdfs/best-research-cell-efficiencies.pdf>.
2. Leijtens, T., Bush, K. A., Prasanna, R. & McGehee, M. D. Opportunities and challenges for tandem solar cells using metal halide perovskite semiconductors. *Nat. Energy* **3**, 828–838 (2018).
3. Lal, N. N. *et al.* Perovskite tandem solar cells. *Adv. Energy Mater.* **7**, 1602761 (2017).
4. Jošt, M., Kegelman, L., Korte, L. & Albrecht, S. Monolithic perovskite tandem solar cells: A review of the present status and advanced characterization methods toward 30% efficiency. *Adv. Energy Mater.* **10**, 1904102 (2020).
5. Jeong, J. *et al.* Pseudo-halide anion engineering for  $\alpha$ -FAPbI<sub>3</sub> perovskite solar cells. *Nature* **592**, 381–385 (2021).
6. Xing, G. *et al.* Long-range balanced electron- and hole-transport lengths in organic-inorganic CH<sub>3</sub>NH<sub>3</sub>PbI<sub>3</sub>. *Science (80-)*. **342**, 344–347 (2013).
7. Xing, G. *et al.* Low-temperature solution-processed wavelength-tunable perovskites for lasing. *Nat. Mater.* **13**, 476–480 (2014).
8. Stranks, S. D. *et al.* Electron–hole diffusion lengths exceeding 1 micrometer in an organometal trihalide perovskite absorber. *Science (80-)*. **342**, 341–344 (2013).
9. Lin, Q. *et al.* Electro-optics of perovskite solar cells. *Nat. Photonics* **9**, 106–112 (2014).
10. Niu, G., Guo, X. & Wang, L. Review of recent progress in chemical stability of perovskite solar cells. *J. Mater. Chem. A* **3**, 8970–8980 (2015).
11. Rocks, C. *et al.* Type-I alignment in MAPbI<sub>3</sub> based solar devices with doped-silicon nanocrystals. *Nano Energy* **50**, 245–255 (2018).
12. Aqoma, H. *et al.* Alkyl ammonium iodide-based ligand exchange strategy for high-efficiency organic-cation perovskite quantum dot solar cells. *Nat. Energy*. **9**, 1–9 (2024).
13. Shilpa, G. *et al.* Recent advances in the development of high efficiency quantum dot sensitized solar cells (QDSSCs): A review. *Mater. Sci. Energy Technol.* **6**, 533–546 (2023).
14. Wang, Y. *et al.* Carrier multiplication in perovskite solar cells with internal quantum efficiency exceeding 100%. *Nat. Commun.* **14**, 6293 (2023).
15. Sahu, A., Garg, A. & Dixit, A. A review on quantum dot sensitized solar cells: Past, present and future towards carrier multiplication with a possibility for higher efficiency. *Sol. Energy* **203**, 210–239 (2020).
16. Ding, C. *et al.* Over 15% efficiency PbS quantum-dot solar cells by synergistic effects of three interface engineering: Reducing nonradiative recombination and balancing charge carrier extraction. *Adv. Energy Mater.* **12**, 2201676 (2022).
17. Velusamy, T. *et al.* Ultra-small CuO nanoparticles with tailored energy-band diagram synthesized by a hybrid plasma-liquid process. *Plasma Process. Polym.* **14**, 1–8 (2017).
18. Haq, A. U. *et al.* Controlling the energy-level alignment of silicon carbide nanocrystals by combining surface chemistry with quantum confinement. *J. Phys. Chem. Lett.* **11**, 1721–1728 (2020).
19. Carolan, D. *et al.* Environmentally friendly nitrogen-doped carbon quantum dots for next generation solar cells. *Sustain. Energy Fuels* **1**, 1611–1619 (2017).
20. Padmanaban, D. B. *et al.* Understanding plasma-ethanol non-equilibrium electrochemistry during the synthesis of metal oxide quantum dots. *Green Chem.* **23**, 3983–3995 (2021).
21. Sulas-Kern, D. B., Miller, E. M. & Blackburn, J. L. Photoinduced charge transfer in transition metal dichalcogenide heterojunctions-towards next generation energy technologies. *Energy Environ. Sci.* **13**, 2684–2740 (2020).
22. Alnaqbi, W., Rezk, A., Alhammedi, A. & Nayfeh, A. Fabrication of a chemically exfoliated 2D MoS<sub>2</sub> nanoparticle based solar cell. *Conf. Rec. IEEE Photovolt. Spec. Conf.* **2022-June**, 12–14 (2022).
23. Mak, K. F., Lee, C., Hone, J., Shan, J. & Heinz, T. F. Atomically thin MoS<sub>2</sub>: A new direct-gap semiconductor. *Phys. Rev. Lett.* **105**, 2–5 (2010).
24. Splendiani, A. *et al.* Emerging photoluminescence in monolayer MoS<sub>2</sub>. *Nano Lett.* **10**, 1271–1275 (2010).
25. Thomas, N. *et al.* 2D MoS<sub>2</sub>: Structure, mechanisms, and photocatalytic applications. *Mater. Today Sustain.* **13**, 100073 (2021).
26. Yuan, Y. *et al.* Recent advances and perspectives of MoS<sub>2</sub>-based materials for photocatalytic dyes degradation: A review. *Colloids Surfaces A Physicochem. Eng. Asp.* **611**, 125836 (2021).
27. Meng, X., Li, Z., Zeng, H., Chen, J. & Zhang, Z. MoS<sub>2</sub> quantum dots-interspersed Bi<sub>2</sub>WO<sub>6</sub> heterostructures for visible light-induced detoxification and disinfection. *Appl. Catal. B Environ.* **210**, 160–172 (2017).
28. Han, B. & Hu, Y. H. MoS<sub>2</sub> as a co-catalyst for photocatalytic hydrogen production from water. *Energy Sci. Eng.* **4**, 285–304 (2016).

29. Luo, Z. *et al.* Enhancing the efficiency of perovskite solar cells through interface engineering with MoS<sub>2</sub> quantum dots. *Nanomaterials*. **12**, 3079 (2022).
30. Zhang, Z. *et al.* Size-tunable MoS<sub>2</sub> nanosheets for controlling the crystal morphology and residual stress in sequentially deposited perovskite solar cells with over 22.5% efficiency. *J. Mater. Chem. A* **10**, 3605–3617 (2022).
31. Jiang, L. L. *et al.* Flower-like MoS<sub>2</sub> nanocrystals: A powerful sorbent of Li<sup>+</sup> in the Spiro-OMeTAD layer for highly efficient and stable perovskite solar cells. *J. Mater. Chem. A* **7**, 3655–3663 (2019).
32. Aranda Alonso, C. *et al.* Overcoming ionic migration in perovskite solar cells through alkali metals. *Joule* **8**, 241–254 (2024).
33. Alexander V. Naumkin, Anna Kraut-Vass, Stephen W. Gaarenstroom, and C. J. P. NIST X-ray photoelectron spectroscopy (XPS) database, version 3.5. <https://doi.org/10.18434/T4T88K>.
34. Jana, A., Ba, Q., Nissimagoudar, A. S. & Kim, K. S. Formation of a photoactive quasi-2D formamidinium lead iodide perovskite in water. *J. Mater. Chem. A* **7**, 25785–25790 (2019).
35. Amelot, D. *et al.* Revealing the band structure of FAPI quantum dot film and its interfaces with electron and hole transport layer using time resolved photoemission. *J. Phys. Chem. C* **124**, 3873–3880 (2020).
36. Huang, W., Manser, J. S., Kamat, P. V. & Ptasinska, S. Evolution of chemical composition, morphology, and photovoltaic efficiency of CH<sub>3</sub>NH<sub>3</sub>PbI<sub>3</sub> perovskite under ambient conditions. *Chem. Mater.* **28**, 303–311 (2016).
37. Huang, S. *et al.* Morphology evolution and degradation of CsPbBr<sub>3</sub> nanocrystals under blue light-emitting diode illumination. *ACS Appl. Mater. Interfaces* **9**, 7249–7258 (2017).
38. Acik, M., Park, I. K., Koritala, R. E., Lee, G. & Rosenberg, R. A. Oxygen-induced defects at the lead halide perovskite/graphene oxide interfaces. *J. Mater. Chem. A* **6**, 1423–1442 (2018).
39. Rocks, C., Svrcek, V., Maguire, P. & Mariotti, D. Understanding surface chemistry during MAPbI<sub>3</sub> spray deposition and its effect on photovoltaic performance. *J. Mater. Chem. C* **5**, 902–916 (2017).
40. Naumkin, A. V., Ann, K.-V., Gaarenstroom, S. W., Powell, C. J. NIST X-ray photoelectron spectroscopy database. <https://srdata.nist.gov/xps/>.
41. Clayton, C. R. & Lu, Y. C. Electrochemical and XPS evidence of the aqueous formation of Mo<sub>2</sub>O<sub>5</sub>. *Surf. Interface Anal.* **14**, 66–70 (1989).
42. Spevack, A. N. S. M. Thermal reduction of molybdenum trioxide. *J. Phys. Chem.* **96**, 9029–9035 (1992).
43. Pratt, A. R., Muir, I. J. & Nesbitt, H. W. X-ray photoelectron and Auger electron spectroscopic studies of pyrrhotite and mechanism of air oxidation. *Geochim. Cosmochim. Acta* **58**, 827–841 (1994).
44. Smart, R. S. C., Skinner, W. M. & Gerson, A. R. XPS of sulphide mineral surfaces: Metal-deficient, polysulphides, defects and elemental sulphur. *Surf. Interface Anal.* **28**, 101–105 (1999).
45. Baby, M. & Kumar, K. R. Synthesis and characterisation of MoS<sub>2</sub> quantum dots by liquid nitrogen quenching. *Mater. Sci. Tech.* **0836**, 1416–1427 (2019).
46. Li, B. *et al.* Preparation of monolayer MoS<sub>2</sub> quantum dots using temporally shaped femtosecond laser ablation of bulk MoS<sub>2</sub> targets in water. 1–12 (2017). <https://doi.org/10.1038/s41598-017-10632-3>.
47. Benson, J., Li, M., Wang, S., Wang, P. & Papakonstantinou, P. Electrocatalytic hydrogen evolution reaction on edges of a few layer molybdenum disulfide nanodots. (2015). <https://doi.org/10.1021/acsami.5b03399>.
48. Imran, M. & Khan, N. A. Perovskite phase formation in formamidinium–methylammonium lead iodide bromide (FAPbI<sub>3</sub>)<sub>1-x</sub>(MAPbBr<sub>3</sub>)<sub>x</sub> materials and their morphological, optical and photovoltaic properties. *Appl. Phys. A Mater. Sci. Process.* **125**, 1–9 (2019).
49. Taylor, A. D. *et al.* A general approach to high-efficiency perovskite solar cells by any antisolvent. *Nat. Commun.* <https://doi.org/10.1038/s41467-021-22049-8> (2021).

## Acknowledgements

This work was supported by the Department for Economy-Northern Ireland (award n.US146), Prof Mariotti's JSPS Invitation and Bridge Fellowships and EPSRC (EP/R008841/1, EP/K022237/1, EP/M024938/1).

## Author contributions

AUK carried out experiments, drafted and contributed to the manuscript. BA and CMcD carried out some of the experiments and contributed to the manuscript. PP produced the MoS<sub>2</sub> quantum dots, contributed to the manuscript. VS and DM contributed to the idea, provided funding and contributed to the manuscript.

## Competing interests

The authors declare no competing interests.

## Additional information

**Supplementary Information** The online version contains supplementary material available at <https://doi.org/10.1038/s41598-024-72037-3>.

**Correspondence** and requests for materials should be addressed to A.U.K. or D.M.

**Reprints and permissions information** is available at [www.nature.com/reprints](http://www.nature.com/reprints).

**Publisher's note** Springer Nature remains neutral with regard to jurisdictional claims in published maps and institutional affiliations.

**Open Access** This article is licensed under a Creative Commons Attribution 4.0 International License, which permits use, sharing, adaptation, distribution and reproduction in any medium or format, as long as you give appropriate credit to the original author(s) and the source, provide a link to the Creative Commons licence, and indicate if changes were made. The images or other third party material in this article are included in the article's Creative Commons licence, unless indicated otherwise in a credit line to the material. If material is not included in the article's Creative Commons licence and your intended use is not permitted by statutory regulation or exceeds the permitted use, you will need to obtain permission directly from the copyright holder. To view a copy of this licence, visit <http://creativecommons.org/licenses/by/4.0/>.

© The Author(s) 2024